Finescale Vertical Structure of a Cold Front as Revealed by an Airborne Doppler Radar

BART GEERTS, RICK DAMIANI, AND SAMUEL HAIMOV

University of Wyoming, Laramie, Wyoming

(Manuscript received 30 July 2004, in final form 11 November 2004)

ABSTRACT

In the afternoon of 24 May 2002, a well-defined and frontogenetic cold front moved through the Texas panhandle. Detailed observations from a series of platforms were collected near the triple point between this cold front and a dryline boundary.

This paper primarily uses reflectivity and Doppler velocity data from an airborne 95-GHz radar, as well as flight-level thermodynamic data, to describe the vertical structure of the cold front as it intersected with the dryline. The prefrontal convective boundary layer was weakly capped, weakly sheared, and about 2.5 times deeper than the cold-frontal density current.

The radar data depict the cold front as a fine example of an atmospheric density current at unprecedented detail (~40 m). The echo structure and dual-Doppler-inferred airflow in the vertical plane reveal typical features such as a nose, a head, a rear-inflow current, and a broad current of rising prefrontal air that feeds the accelerating front-to-rear current over the head. The 2D cross-frontal structure, including the frontal slope, is highly variable in time or alongfront distance. Along this slope horizontal vorticity, averaging ~0.05 s^{-1}, is generated baroclinically, and the associated strong cross-front shear triggers Kelvin–Helmholtz (KH) billows at the density interface. Some KH billows occupy much of the depth of the density current, possibly even temporarily cutting off the head from its trailing body.

1. Introduction

In the afternoon of 24 May 2002, a cold front–dryline intersection was intercepted over the southern Great Plains by an armada of mobile observing platforms as part of the International H_2O Project (IHOP_2002; Weckwerth et al. 2004). The objective of the mission was to capture the initiation of thunderstorms in the vicinity of these boundaries. In the region of detailed observations, the cold front penetrated under the moist air east of the dryline. Deep convection broke out a few tens of kilometers east of this region, clearly ahead of the well-defined surface cold front. This paper does not attempt to explain the timing or location of this convective initiation. Rather, it describes the meso-γ and microscale structure of this cold front, with an emphasis on the *vertical airflow structure*, as documented by airborne radar data.

Corresponding author address: Dr. Bart Geerts, Dept. of Atmospheric Sciences, University of Wyoming, Laramie, WY 82071. E-mail: geerts@uwyo.edu

It has long been postulated that on the meso-γ scale the cold air associated with a cold front may assume the vertical structure of a *density* (or *gravity*) *current* (Fig. 1). Such a current results when two fluids of different density are juxtaposed. Because of negative buoyancy, the denser fluid will penetrate below the less dense fluid in the form of a shallow current with an elevated head and a turbulent wake (Benjamin 1968). Atmospheric density currents have received a great deal of attention (e.g., Simpson 1987), and they have been invoked in the interpretation of a range of mesoscale phenomena, including thunderstorm-generated gust fronts (Charba 1974; Wakimoto 1982; Mueller and Carbone 1987; Mahoney 1988), sea breezes (Abbs and Physick 1992), land breezes (Schoenberger 1984), katabatic winds spreading over level terrain (Bromwich et al. 1992), and also cold fronts (Clarke 1961; Carbone 1982; Hobbs and Persson 1982; Shapiro 1984; Shapiro et al. 1985; Bond and Fleagle 1985; Garratt 1988; Lemaitre et al. 1989; Nielsen and Neilley 1990; Trier et al. 1990; Bond and Shapiro 1991; Hakim 1992; Roux et al. 1993; Koch and Clark 1999; Wakimoto and Bosart 2000). Numerical experiments have shown that the de-

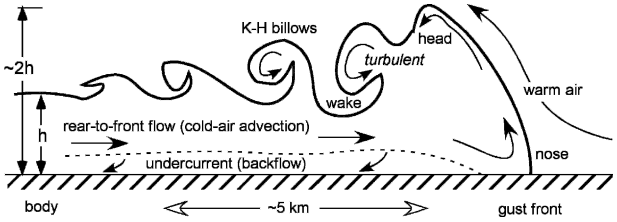

FIG. 1. Schematic view of a density or gravity current (adapted from several sources including Simpson 1969; Charba 1974; Droegemeier and Wilhelmson 1987; and Mueller and Carbone 1987).

tailed vertical structure of atmospheric density currents is sensitive to the ambient shear and stratification (e.g., Xue et al. 1997; Xue 2000, 2002; Liu and Moncrieff 2000).

While density currents have been described in detail by means of numerical simulations and laboratory experiments (e.g., Simpson 1969; Simpson and Britter 1980), *their existence in the atmosphere mainly has been inferred rather than observed*, as the resolution of the observations generally has been too coarse. Some studies do document the head and trailing billows associated with a density current (e.g., Intrieri et al. 1990; Mueller and Carbone 1987; Wakimoto and Bosart 2000), but not nearly at the resolution presented here or in numerical studies. The Doppler lidar study by Intrieri et al. (1990) uses a grid spacing of 50 m in the vertical and 300 m in the horizontal. Mueller and Carbone (1987) performed a dual-Doppler synthesis based on two X-band radars with a baseline of 13 km and a grid spacing of 200 m in three dimensions. The grid resolution used in the current study is less than 40 m in two dimensions.

The processing of the airborne radar data is discussed in section 2. The mesoscale environment in which the cold front evolved is summarized in section 3. Section 4 focuses on aircraft in situ data analyses, while section 5 describes the radar-derived airflow in vertical transects across the cold front.

2. Airborne W-band single- and dual-Doppler analysis

The Wyoming Cloud Radar (WCR) is a 95-GHz (3 mm) Doppler radar (Pazmany et al. 1994). During IHOP the WCR was installed on board the University of Wyoming King Air (UWKA) aircraft, configured for two dual-beam configurations (Fig. 2). The first one is a profiling mode, using both nadir and zenith beams simultaneously. The second one uses the nadir beam in conjunction with a second downward-looking beam

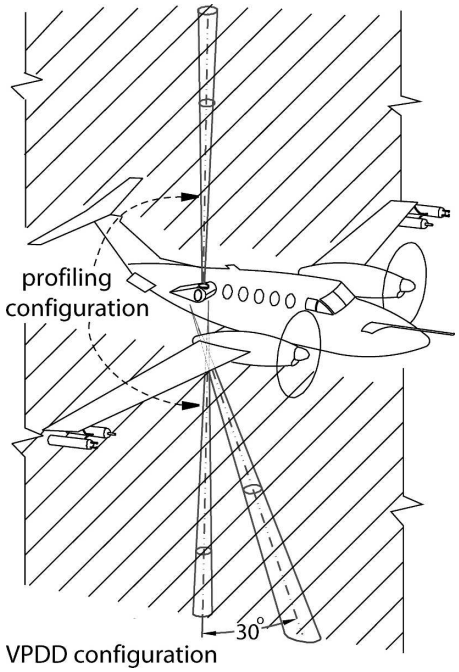

FIG. 2. Radar beam directions on the UWKA aircraft, as used in this study. The two downward beams allow VPDD synthesis, while the up and down beams provide a radar profile, centered at flight level. The first gate for each antenna is at a range of about 100 m.

slanted 30° forward of nadir. The profiling mode allows near-vertical velocities to be measured within 100–130 m above and below the aircraft (Geerts and Miao 2005), while the second mode, referred to as the vertical plane dual-Doppler (VPDD) mode, allows the velocity components in two dimensions along the flight track to be retrieved. If the aircraft flight attitude is relatively constant (i.e., deviations from the mean in roll and yaw are less than ±5°), then the nadir beam resamples the same volume observed by the downward-slanted beam after a short time delay. The two Doppler velocity measurements can be combined to give the horizontal and vertical velocity components in a quasi-vertical plane aligned with the aircraft track (appendix A). The dual-Doppler Cartesian grid has a resolution of about 35 × 35 m^2 in the horizontal (along-track) and vertical directions. During IHOP_2002, the WCR generally operated in profiling/VPDD mode on flight legs below/above 700 m AGL. The WCR unambiguous velocity limits were ±15.8 m s^{-1}. The radar minimum detectible signal at 1-km range was in the proximity of −28 dBZ.

The WCR echoes in the optically clear convective boundary layer (CBL) are believed to be dominated by small insects (Vaughn 1985; Geerts and Miao 2005). Small insects are weak flyers and tend to advect with the wind, hence the term "aerial plankton" (Drake and

Farrow 1988; Russell and Wilson 1997). Thus the retrieved horizontal velocity should be unbiased. It is not clear how well the retrieved vertical echo motion represents vertical air motion. Small insects tend to oppose the updraft in which they become embedded (Geerts and Miao 2005). This seems to be the only viable explanation for the existence and persistence of fine lines, where the echo strength is some 10–30 dBZ above values observed elsewhere in the fair-weather CBL (Wilson et al. 1994; Russell and Wilson 1997), implying insect concentrations of one to three orders of magnitude higher than background values. Passive tracers would simply diverge near the top of the CBL and disperse. Hence the CBL is known as the "mixed" layer. A series of IHOP_2002 flight legs in the fair-weather CBL (i.e., far away from fine lines) suggest that small insects move down relative to the ambient vertical air motion at 0.5 ± 0.2 m s^{-1} on average, and that this downward motion increases in updrafts, at nearly half the updraft speed itself (Geerts and Miao 2005). Small insects may move down either actively, or by folding their wings and falling down at their "terminal velocity." Which of these two methods is the fastest depends on the Reynolds number acting on the insect, but it is probably limited to ~2 m s^{-1} (Pedgley 1982). Thus it is conceivable that the rate of opposition of microinsects to updrafts has a ceiling. Geerts and Miao (2005) did not find such ceiling, but their assessment of insect vertical motion applies to the fair-weather CBL. The updrafts along a cold front may be stronger and more sustained than those associated with thermals. In short, in order to obtain the best-guess vertical air motion ($w_{\mathrm{wcr,air}}$), we adjust the echo vertical motion ($w_{\mathrm{wcr,insects}}$) for insect motion by means of Eq. (2) in Geerts and Miao (2005):

$$w_{\mathrm{wcr,air}} = \min\langle 1.96 w_{\mathrm{wcr,insects}} + 0.82, w_{\mathrm{wcr,insects}} + 1.5\rangle \ \mathrm{m\ s^{-1}}. \quad (1)$$

The first term is a linear regression based on vertical velocity comparisons between the UWKA gust probe and first-gate WCR data above and below the aircraft. The second term constrains this correction (i.e., the incremental upward motion) to 1.5 m s^{-1}. Here $w_{\mathrm{wcr,insects}}$ is the scatterer vertical motion (appendix A), $w_{\mathrm{wcr,air}}$ is the best-guess air vertical motion, and min() takes the minimum of its arguments.

How accurate are the resulting air velocities? One source of uncertainty is the temporal evolution of the scattering features (at a resolution of ~35 m) between the two radar illuminations. The airborne dual-Doppler velocity retrieval method is feasible as long as the volume scanned by one of the beams is observed by the other in a time interval shorter than the characteristic evolution time scale of the scattering volume. With a beam-to-beam time difference of 6 s per 1 km from the aircraft, this condition should be satisfied at typical WCR ranges (usually no more than 3 km). But clearly this error increases with range. Other error sources include both rapid aircraft attitude variations and the cross-track wind. The first results in an irregular spacing and alignment between adjacent beams, with consequent degradation of the vertical resolution. The second plays a role in the removal of the horizontal wind component from the near-vertical radial wind; the best-guess horizontal wind profile is used in the solution of the velocity decomposition problem (see appendix A). The roll and yaw (sideslip) standard deviations for the flight segments used here were within 2°. The overall uncertainty in the calculated velocities for the 24 May data is estimated to be in the order of 1 m s^{-1} at a range of 1 km and for WCR signal-to-noise ratios greater than 0 dB.

3. Mesoscale evolution

In the afternoon of 24 May 2002, a SW–NE-oriented cold front approached a nearly stationary, north–south-oriented dryline near Shamrock, near the eastern margin of the Texas panhandle (Weckwerth et al. 2004; Wakimoto et al. 2006). This front was weak in the morning hours, but frontogenesis occurred during the daytime as the cold sector remained covered by a vast stratus cloud deck (Fig. 3), a process that has been observed elsewhere (e.g., Miller et al. 1996). A sharp contrast in equivalent potential temperature (θ_e) was present at 1800 UTC mainly near the Oklahoma panhandle (Fig. 4). Differential horizontal advection of θ_e during 0600–1800 UTC clearly contributed to the sharpening θ_e gradient. The center of the low-level cyclonic circulation was in the northern Texas panhandle, just north of the intensive observations, and a 1.2×10^{-4} s^{-1} center of positive relative vorticity was found over eastern Colorado at 300 mb, associated with a well-defined short-wave trough (Fig. 4).

The front was mostly stationary in the morning hours (1000–1400 UTC), but it accelerated thereafter. The convergence along the cold front was weak between 1500 and 1900 UTC, at least around the Amarillo Next-Generation Weather Radar (NEXRAD; 143 km west of Shamrock): a clearly defined fine line did not develop there until 2000 UTC, about 4 h *after* frontal passage at the radar site. Similarly, radar and surface station data do not reveal a dryline until about 1930 UTC, but this may be due to the remoteness of the surrounding radars and the paucity of operational weather stations in the Texas panhandle: mobile meso-

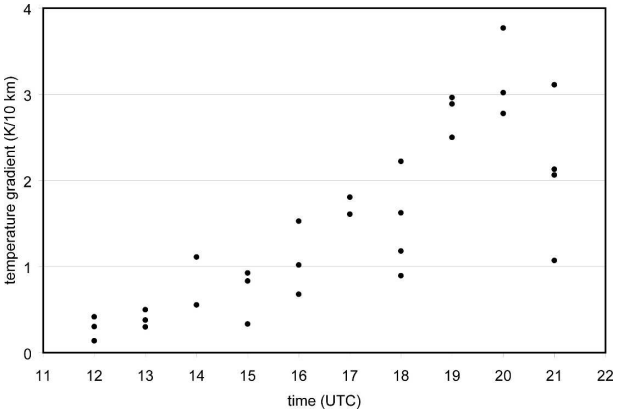

FIG. 3. Change of temperature gradient ($\Delta T/\Delta x$) over time during 24 May 2002 in the Texas panhandle and western Oklahoma. Temperatures are obtained from the Oklahoma Mesonet and the National Weather Service network. Here Δx is computed as the shortest distance between a station in the cold air and the cold front. The location of the latter is fine-tuned based on a fine line observed in the displays of the Amarillo and Vance, TX, NEXRAD radars and S-band dual-polarization Doppler radar (S-Pol), although between 1600 and 1800 UTC none of the radars clearly locates this fine line. The value of ΔT is obtained from the station in the cold air, and the closest station in the warm air. Mobile mesonet temperatures are not included.

net and mobile ground-based radars confirm the presence of a weak dryline boundary from about 1840 UTC, and the Naval Research Laboratory (NRL) P-3 with Electra Doppler Radar (ELDORA) manages to track this dryline from about 1900 UTC (Wakimoto et al. 2006).

A 1906 UTC Mobile GPS/Loran Atmospheric Sounding System (M-GLASS) sounding on the moist side of the dryline (not shown) shows a well-mixed CBL, with a well-defined top around 2.0 km AGL. The CBL wind is weak, from 160° to 190°, and the wind veers to ~220° just above the CBL, with speeds increasing to 12 m s^{-1}. The sounding does not reach saturation in the CBL, but UWKA observations at this time indicate several cumulus clouds in the upper ~400 m of the CBL, at 7, 15, and 19 km east of the dryline. Eight dropsondes were released by a Learjet aircraft around 2030 UTC from 4700 m MSL along an east–west flight leg located just south of the UWKA flight tracks (Fig. 5). The CBL in the eastern half of this leg has mixing ratio (q) values around 12 g kg^{-1}. This layer is weakly capped at about 1.4 km AGL. The cap has a potential temperature jump $\Delta\theta$ of 1–2 K, a Δq of about -3 g kg^{-1}, and a winds veering from southeasterly to southwesterly. This shallow cap becomes better defined toward the east, where it caps abundant stratocumulus clouds, according to UWKA forward camera footage.

The low-level moisture gradient and confluence between sondes 3 and 4 (2032–2035 UTC) suggests the presence of a dryline at the surface. Dropsonde 3 has a remarkably deep mixed layer (about 2.6 km deep), which is drier ($8 < q < 9$ g kg^{-1}) than that in sonde 4. Also, the near-surface wind has a westerly component (Fig. 5). The (q, θ) of the air in this CBL is similar to that in the southwesterly current above the dryline; thus presumably this is one air mass advected over the dryline.

A second, stronger stable layer ($\Delta\theta$ of ~3 K) is present near 2.4 km AGL above this air mass. This cap extends west of the dryline and is better defined at sounding 3 than on the moist side of the dryline, because of surface-driven convective mixing and/or mesoscale frontogenetical forcing. Near the top of the deep mixed layer just west of the dryline (sounding 3), the relative humidity peaks at 91%.

A marked humidity gradient is present farther west, above the cold-frontal surface between dropsonde 2 ($q \sim 2$ g kg^{-1}) and the Mobile Cross-Chain Loran Atmospheric Sounding System (M-CLASS) sounding ($q \sim 8$ g kg^{-1}), between 1.4 and 2.2 km AGL. This boundary also separates warmer air to the west from ~2 K cooler air to the east and is convergent in the east–west direction. It is marked as an "elevated dryline" in Fig. 5. Remotely sensed humidity data from the Lidar Atmospheric Sensing Experiment (LASE) instrument, aboard an aircraft following exactly the same track as the dropsonde aircraft, confirm the existence of this sharp humidity boundary above the cold front (Wakimoto et al. 2006). The UWKA never traveled far enough west to sample it. This boundary may be due to frontogenetical vertical motion, with subsidence to the NW and uplift to the SE. Because just east of this elevated dryline potential instability exists [$(d\theta_e/dz) < 0$] and the air is close to saturation, such uplift would lead to deep convection. In fact θ_e decreases some 14 K between 2.5 and 3.5 km AGL in sonde 3 (Fig. 5).

We calculate the convective available potential energy (CAPE) and convective inhibition (CIN) of the soundings assuming adiabatic mixing in the lowest 50 mb. The 1906 UTC sounding (east of the dryline) has a CAPE of 1627 J kg^{-1} and a CIN of -45 J kg^{-1}. An M-GLASS sounding was released at 1917 UTC between the surface cold front and the surface dryline. This sounding, the last one released before the cold-frontal passage, only extends up to 340 mb, but it captures the same deep, dry CBL as sonde 3, with a clear cap near 2.5 km AGL. Its CIN is -5 J kg^{-1} and its CAPE is estimated at 1806 J kg^{-1}. Sonde 3, released in the same sector some 30 km farther south at 2032 UTC, has a CIN of -12 J kg^{-1} and a CAPE estimated at 1983 J kg^{-1}. These estimates assume an upper atmosphere

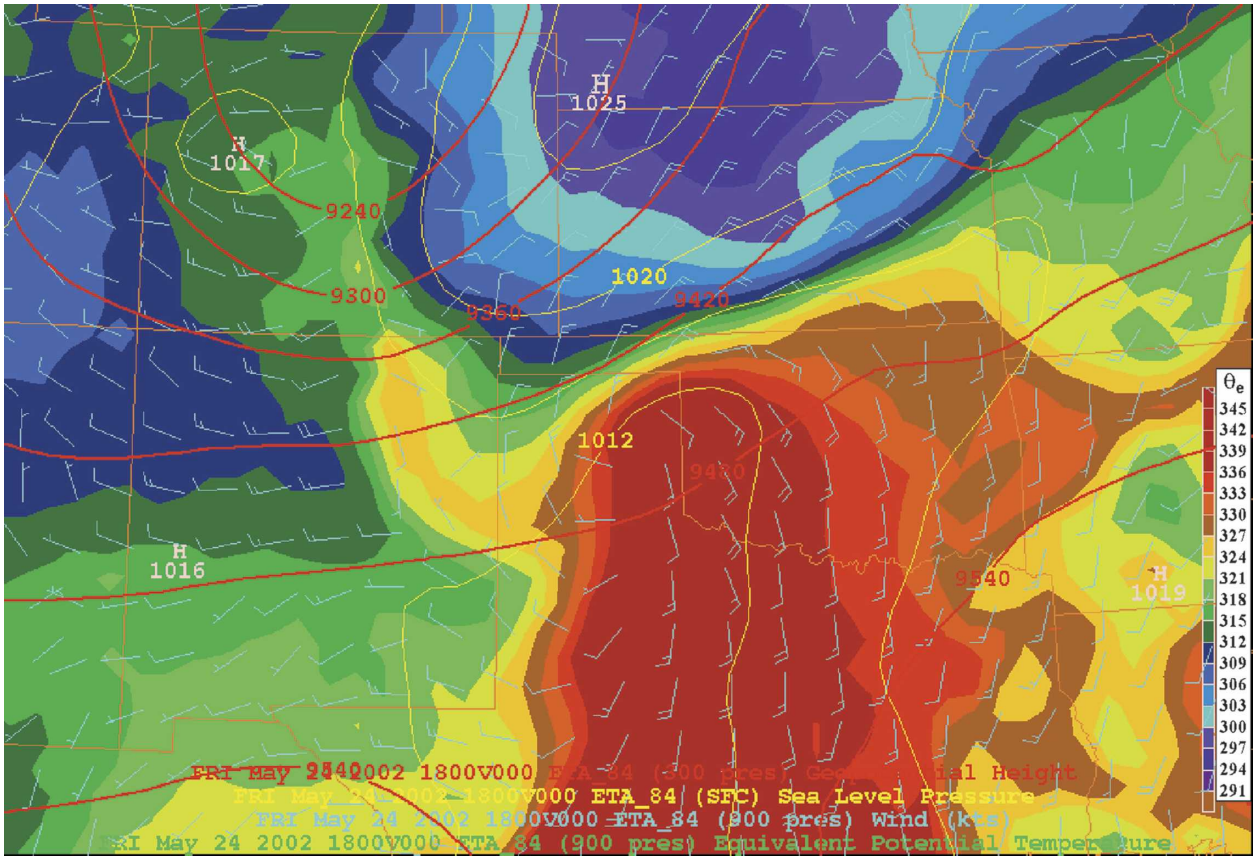

FIG. 4. Synoptic situation at 1800 UTC on 24 May 2002, based on the initial fields of the Eta Model. Shown are the 900-mb equivalent potential temperature (color field), the 900-mb wind barbs (a full barb equals 5 m s^{-1}), the sea level pressure (thin yellow contours), and the 300-mb geopotential height (thick red contours).

(above the highest level with data) from the 1906 UTC full sounding. In short, the triple-point environment was poised for convective initiation.

Shared Mobile Atmospheric Research and Teaching Radar (SMART-R) and mobile mesonet data show that the circulation near the dryline is confluent, and that the dryline echo strength intensifies between 1900 UTC and the time that it is lifted over the cold front. During that period the dryline also moved to the east at about 3 m s^{-1}. The cold front, propagating toward the southeast at a speed of about 7 m s^{-1}, and the developing dryline intersect about 25 km west of the SMART-R located at Shamrock at 2000 UTC (Fig. 6). Mesonet surface observations confirm the presence of three air masses near the "triple point": the postfrontal cool air mass; the warm, moist air east of the dryline, advected from the south; and the warmest and driest air mass, wedged between the cold front and the dryline. Note the elevated dewpoint values in the postfrontal air; in fact they are higher than those east of the dryline (Fig. 6). The high moisture content of the postfrontal air is confirmed by UWKA measurements (e.g., Fig. 8 of Weckwerth et al. 2004) and is consistent with the stratus cloud deck, whose edge trailed the cold front by about 10 km during UWKA observations. The synoptic flow (Fig. 4) suggests that this moisture is drawn from the east and is wrapped around by the cyclonic flow.

The triple point was the focus of intensive observations. ELDORA Doppler wind syntheses indicate that the triple point was the center of a cyclonic circulation and rising air currents (Wakimoto et al. 2006). The UWKA flew multiple legs, 30–50 km long at levels between 150 and 2440 m AGL, crossing both the surface dryline and cold front. The cold front protruded under the dryline, upon which the latter becomes elevated and smeared out, as shown further by radar data.

Deep convection did not break out at the cold front, nor did it break out along the triple point as that point "zipped" southward. Rather, deep convection developed east of the cold front, and the development zipped northward. The first towering cumuli developed around 2010 UTC, just east of the SSW–NNE-oriented dryline,

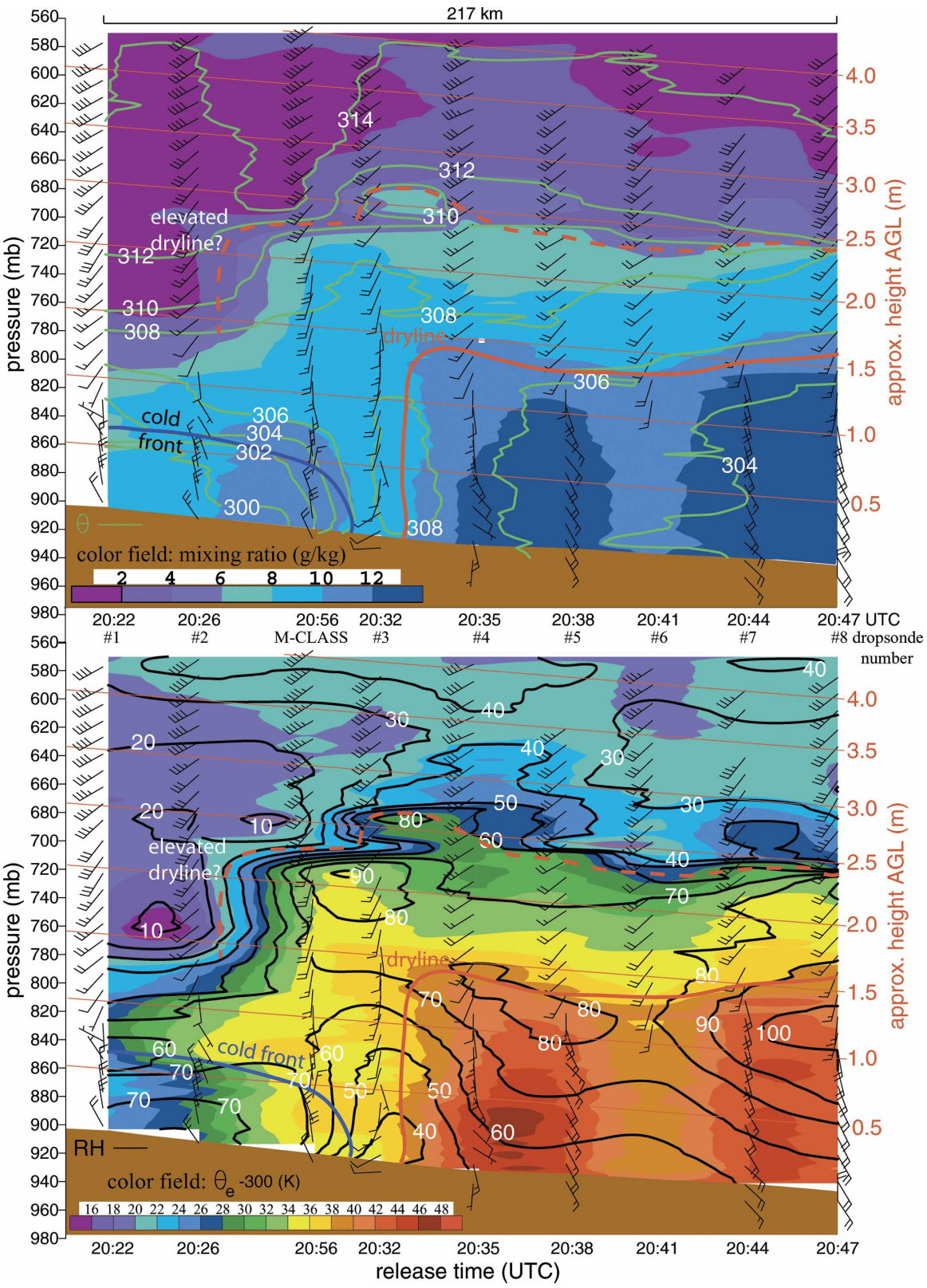

FIG. 5. Cross section across the cold front and dryline, based on a series of sondes dropped between 2022 and 2047 UTC along a west-to-east transect at 35°N, starting near the center of the Texas panhandle. Also included is an M-CLASS sounding released at 2056 UTC. The top transect shows mixing ratio q (g kg^{-1}) and potential temperature θ (K), and the bottom one relative humidity

→

near Childress, about 90 km south of Shamrock (Xue and Martin 2006). Later the deep convection progressed northward, with the first towering cumulus along the final UWKA flight leg at 2113 UTC, some 30 min after the dropsonde data were collected there (Fig. 5). The echo from this first cumulus was weak (<-5 dBZ), indicating that precipitation-size particles had not yet formed. The UWKA forward-looking camera indicates that the congestus penetrated well above the flight level, which was 2.6 km AGL, that is, just above the second stable layer, with even taller cumuli just south of the flight track. This indicates that at this location and time an undiluted parcel rising to 2.5 km was positively buoyant, or at least penetrated through what CIN may have remained. By 2130 UTC a solid line of thunderstorms was present from Childress to the Texas–Oklahoma border east of Shamrock. This line was aligned with the dryline, but as it continued to expand toward the northeast, it became aligned with the cold front.

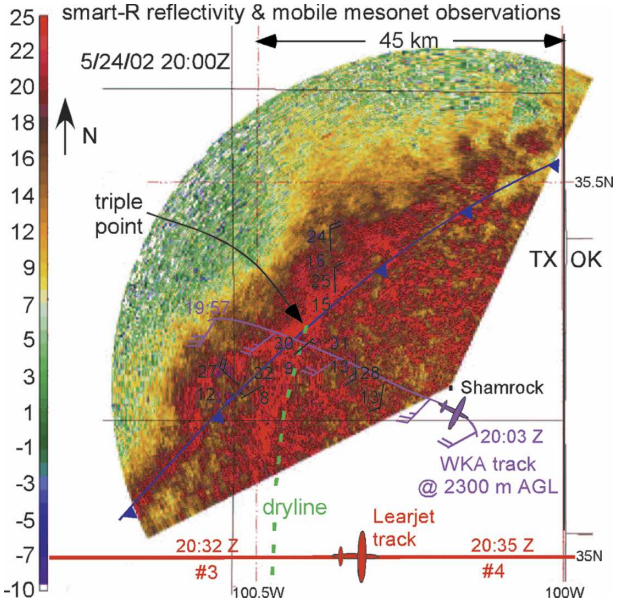

FIG. 6. SMART-R 0.5° elevation reflectivity (dBZ) scan, plus mobile mesonet observations, at 2000 UTC. Also shown are the UWKA track, nearly intersecting the triple point, with flight-level winds at 725 mb, and the Learjet track, with the location of some dropsondes shown in Fig. 5.

4. Finescale aircraft and cloud radar observations

A vertical transect of WCR reflectivity and corresponding in situ measurements across the cold front and primary dryline is shown in Fig. 7. Note that the WCR reflectivity values are much lower than those for a C-band radar (Fig. 6). That is because reflectivity is inferred from power assuming Rayleigh scattering, yet the bulk of the W-band scatterers in the CBL are believed to be in the Mie regime (Geerts and Miao 2005) where the scattering efficiency oscillates with size. At C band, a larger fraction of scatterers are in the Rayleigh regime.

A transect similar to the one in Fig. 7, but about 13 min later, is shown in Fig. 8 of Weckwerth et al. (2004). In both transects the cold-frontal surface clearly slopes toward the cold air, while the dryline echo is upright. Both show a clear discontinuity of θ and q at the cold front. The dryline is marked by sudden moistening ($\Delta q \sim 2$ g kg^{-1}) and some cooling ($\Delta\theta < 1$ K). In terms of buoyancy, the moistening and cooling roughly cancel each other [$\Delta\theta_v \sim 0$ (Fig. 7b)]. In both transects the dryline echo is weaker than the cold front echo, possibly because the $\sim$10 m s^{-1} surface winds behind the cold front pick up and mix more insects and nonbiotic scatterers. The most remarkable difference between the 1935 UTC transect (Fig. 7) and the 1948 UTC transect (Fig. 8 of Weckwerth et al. 2004) regards the depth and shape of the leading edge of the cold-frontal density current. Clearly the morphology of the density current head (Fig. 1) changes rapidly. The WCR data may also witness alongfront variations: laboratory simulations have demonstrated that the leading edge of density currents is marked by a series of clefts and lobes (e.g., Simpson and Britter 1980).

The rapid changes in echo structure are consistent with the variability of vertical air velocity structure. In Fig. 7 an updraft of up to 7 m s^{-1} occurs at the head of the cold front, and several strong up- and downdrafts follow behind. Behind the first, shallow head at $x = 0$ (horizontal axis in Fig. 7), warm, dry air is entrained from above, down to flight level (360 m AGL). This is suggested by the q depression and θ spike at $1.5 < x < 2$ km (Fig. 7a), and the coincident low WCR reflectivity above flight level. This buoyant parcel (Fig. 7b) is about to be propelled upward again by the observed updraft.

←

RH (%) and equivalent potential temperature θ_e (K). Wind vectors are plotted, with a full barb representing 5 m s^{-1}. The cold front and the dryline are shown. The moist air below the dryline (solid red line) is weakly capped near 1.4 km AGL, and a second stable layer is found near 2.4 km AGL (dashed red line). This appears to be the upper limit of an elevated moist layer, whose western limit is quite apparent above the cold-frontal surface.

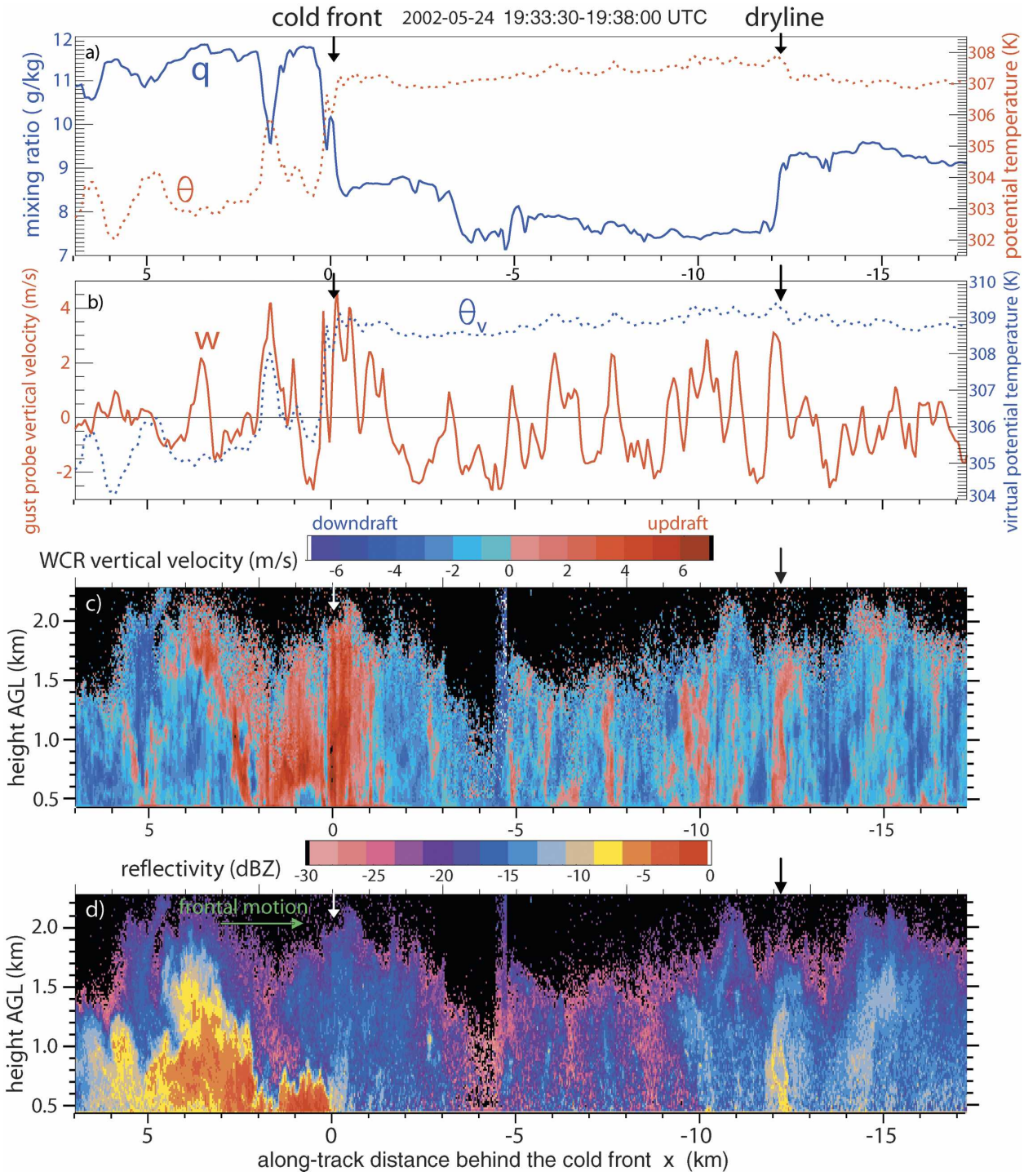

FIG. 7. (a) Mixing ratio and potential temperature, and (b) virtual potential temperature and gust probe vertical velocity, along a flight track at 360 m AGL across the cold front and dryline, around 1935 UTC, displayed at an aspect ratio (height:length) of 2½:1. This cross section cuts across the cold front at an angle of about 35° from the cold-front normal direction. (c), (d) Corresponding WCR vertical velocity and reflectivity above flight level.

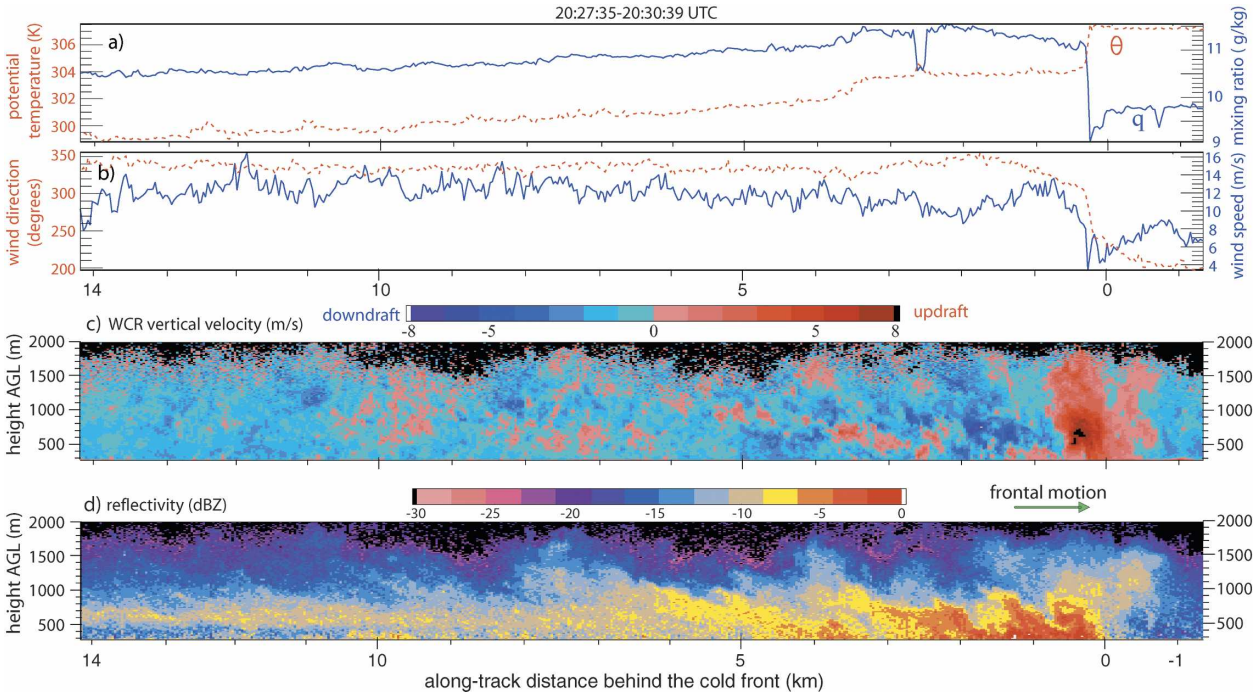

FIG. 8. (a) Mixing ratio and potential temperature, and (b) wind speed and direction along a flight track at 170 m AGL across the cold front, around 2029 UTC. (c), (d) The corresponding WCR vertical velocity and reflectivity fields above flight level. The aspect ratio of the cross sections is exactly 1:1. The angle between this cross section and the cold-front normal direction is less than 20°.

It is not clear whether the strong postfrontal echo at $2 < x < 4$ km in Fig. 7d, up to 1.5 km AGL, contains cold air, in other words whether the head tops at 1.5 km AGL. A flight leg at about 1200 m AGL crosses the cold front at 2025 UTC and encounters two brief surges of cooler, moister air, coincident with WCR plumes up to flight level, but $\Delta\theta < 1$ K, suggesting that this plume has been much diluted. Another flight leg at this level, crossing the cold front at 2054 UTC, does not intercept the cold-frontal surface at all. Other WCR reflectivity transects and photography from aboard the UWKA indicate that the deep cold-frontal plume shown in Fig. 7 is rather rare. The head of the cold front was not deep enough to saturate the air and yield a cloud. Several downward intrusions of ambient air can be seen in the reflectivity transect behind the cold front, and the high variability of θ behind the cold front is an indication of intense mixing between the two different air masses.

The intense mixing behind the cold-frontal head is apparent also in a transect around 2028 UTC (Fig. 8), after the cold front has penetrated under the dryline (the one shown at $x = -12$ km in Fig. 7). A ~700 m wide updraft peaking at 9 m s^{-1} is found at the cold-frontal head. This broad updraft is strongest near the top of the strongest echoes (700–800 m AGL according to Fig. 8d), but it extends to the top of the mixed layer near 2.0 km AGL; that is, it is much deeper than the cold-frontal surface. The updraft peak is trailed by a 5 m s^{-1} downdraft. The curling of the reflectivity in the direction of the wind shear across the cold-frontal surface is indicative of large, breaking Kelvin–Helmholtz (KH) waves.

One of the KH billows, at $x = 2.6$ km, brings drier, warmer air down to flight level, merely 170 m AGL (Fig. 8). Downward curls of low reflectivity tend to correspond with downdrafts. The amplitude of the KH billows and the strength of the updraft/downdrafts near the cold-frontal surface quickly dampen toward the rear. The sloping echo bands above the cold front in Fig. 8d may be detrained echo-rich cool air, or else they may be sheared-out remnants of plumes in the prefrontal CBL. The trailing narrow strip of higher reflectivity around 600–700 m AGL ($x > 8$ km in Fig. 8) is at least partially due to cloud droplets: stratus clouds were present starting at about $x = 8$ km. Video from a forward-facing camera on the UWKA shows a series of low-amplitude cloud bands aligned with the front, presumably due to gravity waves on the cold-frontal surface. The bands merge into a continuous stratus deck farther rearward. WCR reflectivity transects such as that in Fig. 8 indicate that the depth of the trailing body of the density current (h in Fig. 1) is about 800 m. This

agrees with lidar backscatter observations (Wakimoto et al. 2006), and a high-resolution numerical simulation (Xue and Martin 2006).

We now compare some of the observed density current characteristics to theory. Kelvin–Helmholtz instability occurs when the Richardson number Ri is less than 0.25 (Britter and Simpson 1978; Mueller and Carbone 1987). The Ri is the ratio of the stability (N^2) to the shear between two fluids; in other words it compares the potential energy needed to overturn two layers, to the kinetic energy available for it (Holton 2004, p. 283). The Ri for an interfacial layer is

$$\mathrm{Ri} = \frac{N^2}{|\nabla \mathbf{v}|^2}, \tag{2}$$

where is $\mathbf{v}$ the wind vector. Because Ri involves gradients, it is very scale-dependent. Near-surface flight-level data [Figs. 7 and 8, as well as Fig. 8 in Weckwerth et al. (2004)] suggest that the horizontal temperature gradient ($\Delta\theta/\Delta x$) at the cold front is about 3 K over a distance of 100 m along the flight track. If we assume that this gradient is tilted into the vertical, then $N^2 \cong 10^{-3}\ \mathrm{s}^{-2}$. An M-GLASS sounding was released about 2 min after the passage of the cold front, at 2006 UTC. The cold-frontal surface is encountered at about 800 m AGL. Potential temperature and the horizontal wind normal to the cold front are filtered to a height increment of 100 m. Under these conditions, we obtain a maximum stability ($\Delta\theta/\Delta z$) of 3.6 K $(100\ \mathrm{m})^{-1}$ at 800 m AGL, that is, about the same gradient as in the horizontal direction across the front. At the same level and over the same depth, the front-normal shear $|\nabla \mathbf{v}|$ is 0.12 s^{-1}. Thus the minimum Ri is 0.08; that is, the density interface at 800 m AGL is unstable to KH overturning.

The wavelength L of KH billows depends on the depth of the mixed layer h and also on Ri. For Ri $\approx$ 0.1, the ratio $h/L \approx 0.4$ (Thorpe 1973). Assuming a post-frontal mixed-layer depth h of 800 m, the wavelength L should be about 2 km. Figure 8d, and flow field analyses presented in section 5 below, indicate that the wavelength is quite irregular, starting at about 1 km and increasing rearward of the head. Most theoretical and laboratory work on KH billows has focused on linear wave development along a horizontal, sheared density interface, not along the leading edge of a density current. The irregularity of the KH wavelength is consistent with the variable structure of the head and the nonlinear behavior of high-amplitude breaking waves.

The intense mixing can only be sustained by continued front-relative rear-to-front inflow of cool air. The frontal passage is associated with a veering of the wind from southwesterly to northwesterly (Fig. 8), with wind speeds at 170 m between 10 and 13 m s^{-1}, clearly exceeding the speed of the cold front (7 m s^{-1}). Such front-to-rear current is characteristic of a density current (Simpson 1987), and laboratory experiments suggest that it is 40%–50% stronger than the density current speed (Simpson and Britter 1980; Goff 1976), that is, about 9.8–10.5 m s^{-1} in our case, in a fixed reference frame.

Finally, we compare the observed speed of the cold front to the density current speed U_{dc} as inferred from theory and laboratory experiments (Simpson 1987):

$$U_{\mathrm{dc}} = \mathrm{Fr}\sqrt{gh\,\frac{\Delta\theta_v}{\theta_v}} + 0.62U. \tag{3}$$

Here Fr is the Froude number of the prefrontal air, $\Delta\theta_v$ the difference in virtual potential temperature across the density current, and U the prefrontal flow, normal to the density current. In our case, $\Delta\theta_v \approx 4K$ [Figs. 7 and 8, and Fig. 8 in Weckwerth et al. (2004)], and $U \approx -4$ m s^{-1} (Fig. 9). Thus to yield $U_{\mathrm{dc}} = 7$ m s^{-1}, Fr should be about 0.9, which compares well to the values of Fr used in the literature (e.g., Wakimoto 1982; Smith and Reeder 1988).

5. Vertical kinematic structure of the cold front

Four sections of VPDD-derived air motion across the cold front are presented. Two of them are from a low flight level (about 1200 m AGL) and two from a higher altitude (about 2300 m AGL). The former ones clip off parts of the circulation above the density current, but they tend to be more accurate due to the shorter radar range (section 2). The vectors will be shown in a front-relative frame of reference. Also shown are select streamlines and the "horizontal" vorticity field, that is, the component of the vorticity vector normal to the WCR transect. More details on the derivation of the velocity fields are given in appendix B.

The cold front is merely 1.5 km northwest of the primary dryline (Fig. 6) in the cross section shown in Fig. 10. The peak reflectivity values are unusually high (-5 dBZ) near the ground, possibly due to debris and dust that could be seen blowing over some bare fields from the air. The tilt of the warm current rising over the density current, and that of the echo plume associated with it, is close to 45°. Just behind the deep slanted updraft is a pronounced downdraft. At flight level q is some 2 g kg^{-1} higher above the head ($x = 2200$ m), and θ some 4 K lower. Also, the maximum q and minimum θ are about the same values as those encountered at low levels in the prefrontal dry-side CBL. This suggests that air from the prefrontal CBL below is lifted to a height

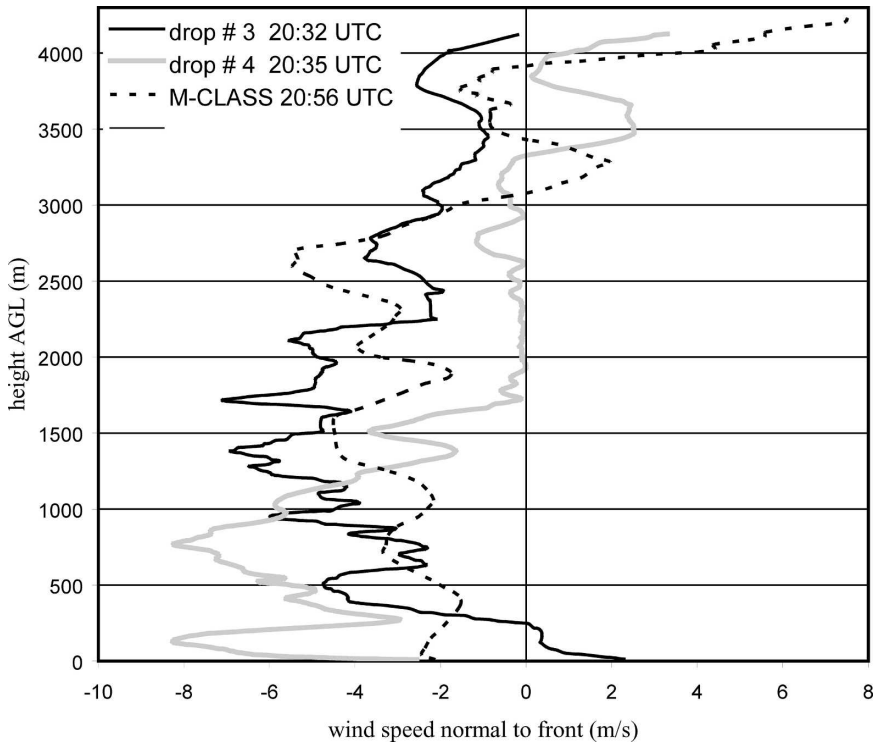

FIG. 9. Wind speed profile normal to the cold front, as inferred from three sondes. Drop 4 was released about 36 km ahead of the cold front, the two others within 15 km of the front. The frame of reference is fixed. Negative values imply flow toward the front.

of 2.3 km AGL, into the stable layer between 2.0 and 2.4 km AGL (section 3). A similar air mass (high q, low θ) is encountered again farther upstream at 2.3 km AGL, above the front (between $3050 < x < 3600$ m in Fig. 10). This appears to be another perturbation in the stable layer, this time not associated with an updraft in the close-range VPDD velocities. Farther to the WNW ($x = 3800$ m), q decreases to 2 g kg^{-1} and θ returns to ~310 K, and several other, weaker high-q, low-θ anomalies follow. These anomalies are negatively buoyant and should subside, as they are not sustained by uplift. Apparently the density current head triggers a trailing gravity wave in the stable layer well above that current. Numerical simulations confirm that a stable layer tends to cap the maximum amplitude of KH billows and that gravity waves can be generated in this layer by an underlying density current [e.g. the "LID1" experiment in Xue (2002)].

The retrieved vector field in Fig. 10 displays much local variability, but in general it appears quite smooth and continuous between grid points, especially in echo-rich areas. The horizontal vorticity of the flow field in Fig. 10 (not shown) peaks in a sloping belt that is nearly coincident with the high-echo belt. The vorticity peaks near the top of the ascent, consistent with the bend in the streamlines. Also note the acceleration of the flow over the density current head, and the merger, just ahead of the head, of the descending upper-CBL air with ascending lower-CBL air.

A second pass over the front, about 10 min later, precisely transects the triple point (Fig. 11), according to SMART-R reflectivity imagery (not shown) and Fig. 4d in Wakimoto et al. (2006). The remnants of the dryline, being lifted over the cold front, may be seen in the reflectivity field (Fig. 11a) and the flow field (Fig. 11b), but not in the in situ observations at 2.3 km AGL. The dryline circulation is most apparent in the vertical velocity field (Fig. 11b), with rising motion to the west, and sinking motion to the east. This circulation is also resolved by a stepped traverse of UWKA gust probe data (C. Ziegler 2004, personal communication).

When a strong density current (i.e., one with a large negative buoyancy or virtual potential temperature deficit) collides with a weaker one, it penetrates under the weaker one, and the remnants of the latter may be seen as a propagating bore on the surface of the strong current (Kingsmill and Crook 2003). In our case the intersection of cold front and dryline can hardly be considered a collision between density currents, because the dryline lacks a substantial buoyancy gradient (Fig.

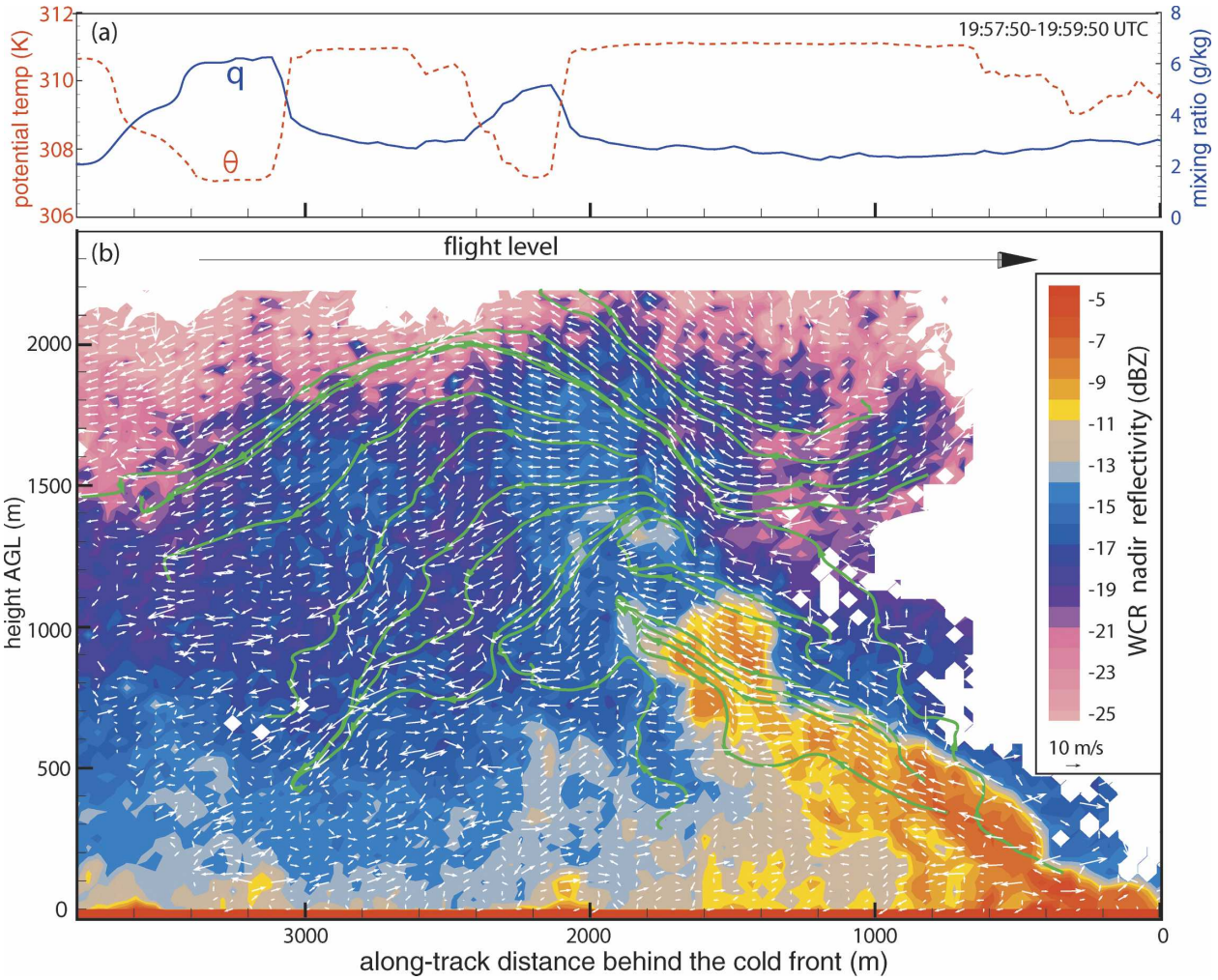

FIG. 10. (a) Flight-level (~2.3 km AGL) mixing ratio and potential temperature for a 290°–110° transect over the cold front at 1958 UTC. (b) Front-relative airflow field below the aircraft (white vectors). The airflow is synthesized from the slant forward and nadir WCR beam radial velocities. The aspect ratio is 1:1; i.e., the vertical axis or vertical component of the vectors are not exaggerated. The grid resolution 35 m × 33 m. The solid green lines with arrows are select streamlines, shown to aid the visualization of the flow. The background color field is nadir beam radar reflectivity. The solid red stripe at the bottom is the ground.

7). Thus the dryline boundary is simply stretched out and diffused in the front-to-rear flow, with no dynamic effect on the cold-frontal surface.

The tilt of the leading edge of the front in Fig. 11 is merely 30°, notwithstanding the orientation of this transect, just ~16° off the normal across the cold front. Near the ground, the edge of the density current appears sharper (stronger reflectivity gradient) and a slightly elevated "nose" appears (Fig. 1). In the upper layers of the cross section the flow is less turbulent, at least at the scales resolved by the VPDD analysis. This is the prefrontal air mass uplifted and accelerated to the rear by the advancing density current.

A remarkably continuous, sloping belt of ascending motion is found at the leading edge of the density current (Fig. 11b). This belt is broad (~500–800 m) and reaches across the full depth of the CBL (nearly 2.0 km). The updrafts average (peak) about 4 m s^{-1} (12 m s^{-1}) in this belt. The maximum downward velocity reaches −10 m s^{-1} at 4500 m behind the density current nose. The vertical velocity field shows some undulations in the top layer (between 2.0 and 2.2 km) above the density current. This, together with flight-level data, is consistent with the stable layer found near 2.0–2.3 km AGL.

The leading edge of the front corresponds with a sloping zone of strong wind shear. The corresponding values of horizontal vorticity are as high as 0.20 s^{-1} (Fig. 11c). In a narrow sloping belt about 1200 m deep that separates updrafts from downdrafts (Fig. 11b) and

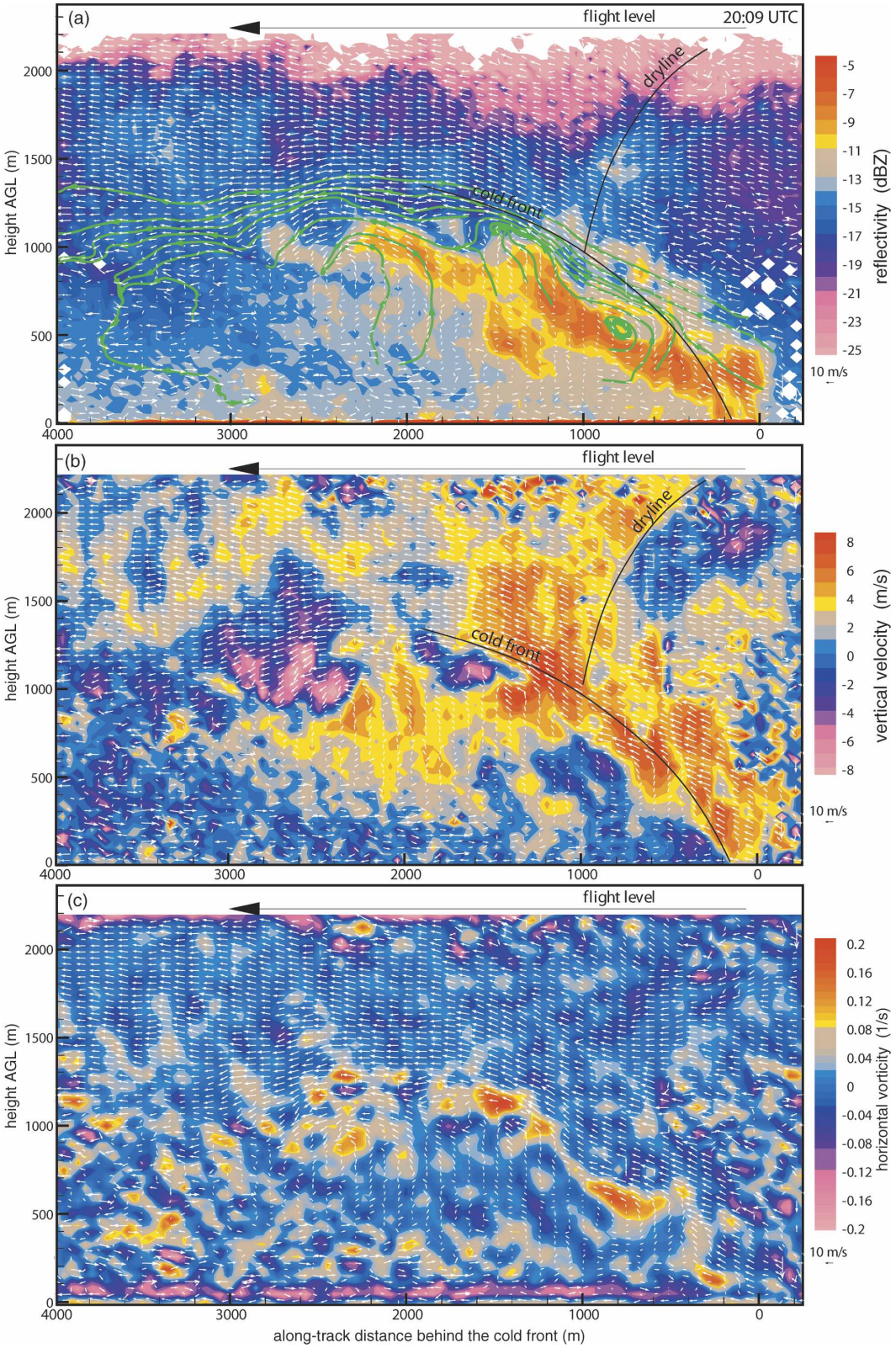

FIG. 11. (a)–(c) As in Fig. 10, but at 2009 UTC, with a flight leg orientation of 344°–164°; (b) and (c) have the same vector field as in (a), except that the background color field in (b) is vertical air motion (m s^{-1}) and in (c) is horizontal vorticity (s^{-1}). Flight-level data are not shown.

in which insects are concentrated (Fig. 11a), the vorticity averages 0.05 s^{-1} (Fig. 11c). These vorticity values are 5–10 times larger than previously reported for an atmospheric density current (Mueller and Carbone 1987) and comparable to the highest radar-measured values in tornadoes (Wurman and Gill 2000). Clearly this vorticity cannot be advected from the warm or cold sides, so it must be locally generated by the buoyancy gradient: ignoring variations in the third dimension (along the cold front), the Lagrangian change in horizontal vorticity η is proportional to the horizontal gradient of buoyancy B (e.g., Rotunno et al. 1988):

$$\frac{D\eta}{Dt} \cong -\frac{\partial B}{\partial x} \cong -\frac{g}{\theta_v}\frac{\partial \theta_v}{\partial x}. \tag{4}$$

UWKA data (e.g., Fig. 7) indicate that $\Delta\theta_v \approx 3K$ on the scale of ~100 m, and thus 0.06 s^{-1} of vorticity, can be generated in one minute. The vorticity generated along the sloping density current head is shed rearward and is "collected into nodes by the KH instability and the [shear] layer is rolled up into billows . . ." (Scorer 1997). Little vorticity exists on average to the right of the density current head in Fig. 11 (only partly shown). Behind the head, the vorticity variability is much larger, and numerous small, mainly positive cores are present. (Here positive vorticity means that the vector points out of the page.) These cores are the result of KH wave breaking; however turbulent kinetic energy (mostly at smaller scales) is probably also generated by the large surface heat fluxes as cold air moves over a soil heated by a high sun. A ~500 m large positive vortex is present near $x = 2200$ m, $z = 1000$ m in Fig. 11c. Smaller vortices appear to be shed from this main vortex, and appear to be advected toward the surface and then forward by the rear inflow. Some vortex structures are strong enough to affect the scatterers' distribution (e.g., at $x = 1600$ m, $x = 2500$ m, both near $z = 1100$ m in Fig. 11a).

The ~100 m deep layer of negative vorticity values near the bottom of Fig. 11c is no artifact; in fact it occurs in the cold air only. This vorticity is generated by surface friction. Clearly the WCR resolution suffices to capture the aerodynamic boundary layer in which, relative to the front, the flow is reversed (the "undercurrent"; Fig. 1).

A low-level VPDD transect across the cold front, about 15 min after it collided with the dryline, is shown in Fig. 12. The remnants of the dryline are believed to be near $x = 3500$ m, with some enhanced reflectivity and an updraft/downdraft couplet just below flight level a moisture gradient at flight level, 1.1 km AGL. The density current head is just tall enough that some cooler air is sampled at flight level, near $1000 < x < 1300$ m (Fig. 12a). That cooler air also contains more water vapor, as documented before (Figs. 7 and 8). The density current nose is well defined, and above it the leading edge slopes back at about 55°, which is much steeper than 15 min earlier (Fig. 11), even though the flight leg orientation is the same.

Unlike previous transects, a second reflectivity maximum is found in the updraft region (near $x = 1500$ m, $z = 600$ m) of a large vortex to the rear, marked as "A" in Fig. 12b. In fact reflectivity values in this updraft inside the gravity current body are higher than those along the sloping head, suggesting that the updraft is sustained (Geerts and Miao 2005). The diameter of vortex A is about 1000 m, and on that scale the horizontal vorticity η, 0.04 s^{-1}, is nearly as large as at the leading edge. Fine streaks in the vorticity field (Fig. 12d), associated with curved cores of stronger ascent (Fig. 12c), appear to be wrapping around vortex A. The circulation around A and the resulting entrainment/detrainment are strong enough that the rear-inflow current becomes much weaker ahead of A. The downdraft to the left of vortex A penetrates to very low levels, which has been observed in other transects (e.g., Fig. 8) and in other studies (e.g., Mahoney 1988).

Pressure variations in KH billows are largely dynamically induced (e.g., Houze 1993, p. 315), and the pressure perturbation (p') in the center of the billows can be estimated from a cyclostrophic balance:

$$\frac{1}{\rho}\frac{\partial p'}{\partial n} = R_s\eta^2, \tag{5}$$

where R_s is the mean radius of curvature of the streamlines around the vortex, n the distance coordinate in the radial direction (positive outward), and ρ the air density. With $\eta = 0.04$ s^{-1} and $R_s = 500$ m, the pressure deficit within circulation A is 4 mb. Pressure deficits can also result from the acceleration of the front-to-rear flow over the head (e.g., Wakimoto 1982): if we assume steady flow and apply the Bernoulli equation along a streamline from the stagnation point ($x = 0$, $z = 0$) to the head of the density current (the bold streamline in Fig. 12b), then the perturbation pressure p' can be estimated as

$$p' = -\frac{\rho V^2}{2}, \tag{6}$$

where V is the wind speed in the front-relative frame of reference. The broad updraft to the right of vortex A (Fig. 12c) may be due to the Bernoulli pressure deficit above the head. Here V is relatively weak along the streamline near $x = 1500$ m, but farther downstream

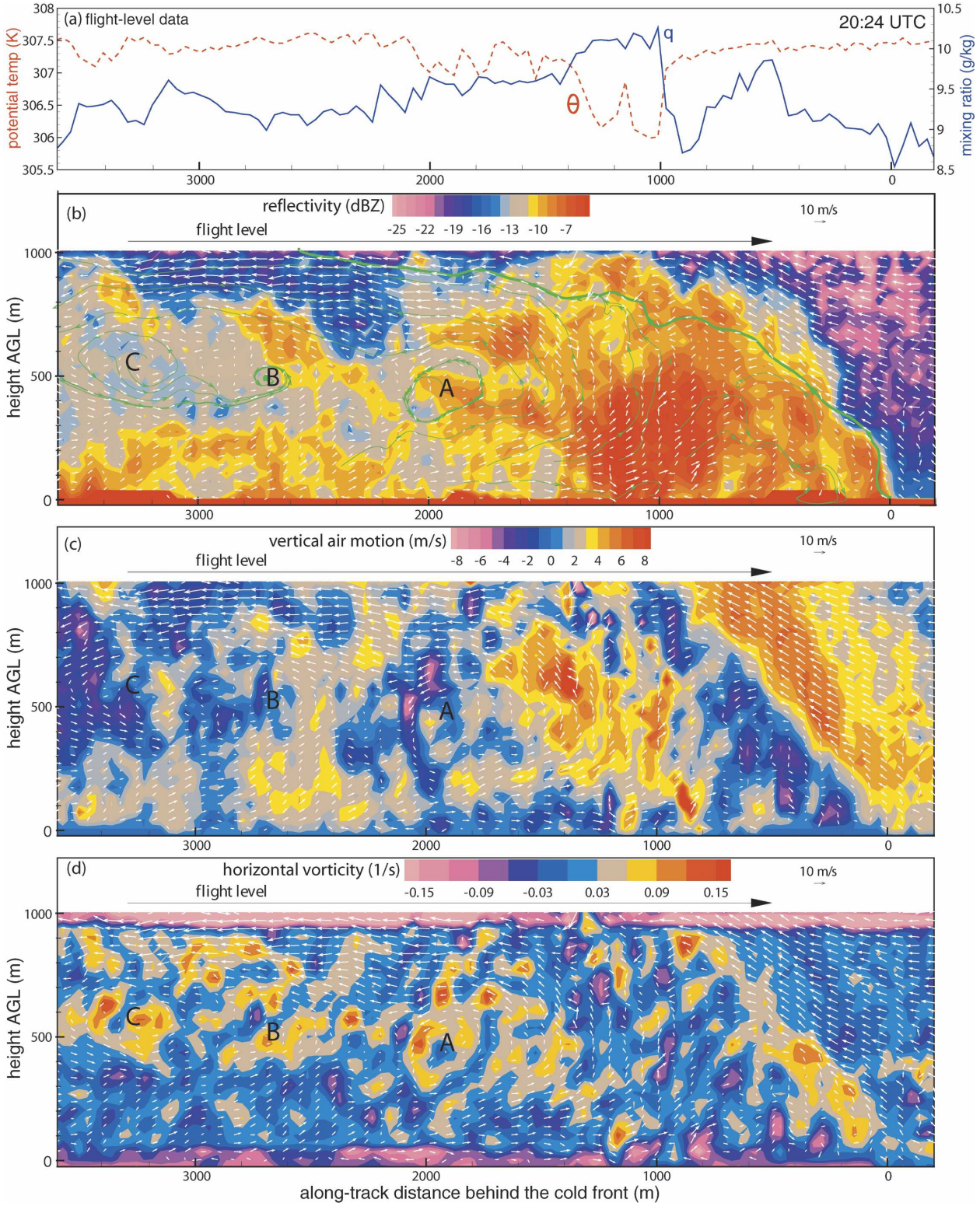

FIG. 12. (a)–(d) As in Fig. 10, but the flight level is ~1.1 km, the flight leg orientation is 344°–164°, and the time is 2024 UTC; (c) and (d) show the same flow field as (b), except that the background color field in (c) is vertical air motion (m s^{-1}) and in (d) is horizontal vorticity (s^{-1}).

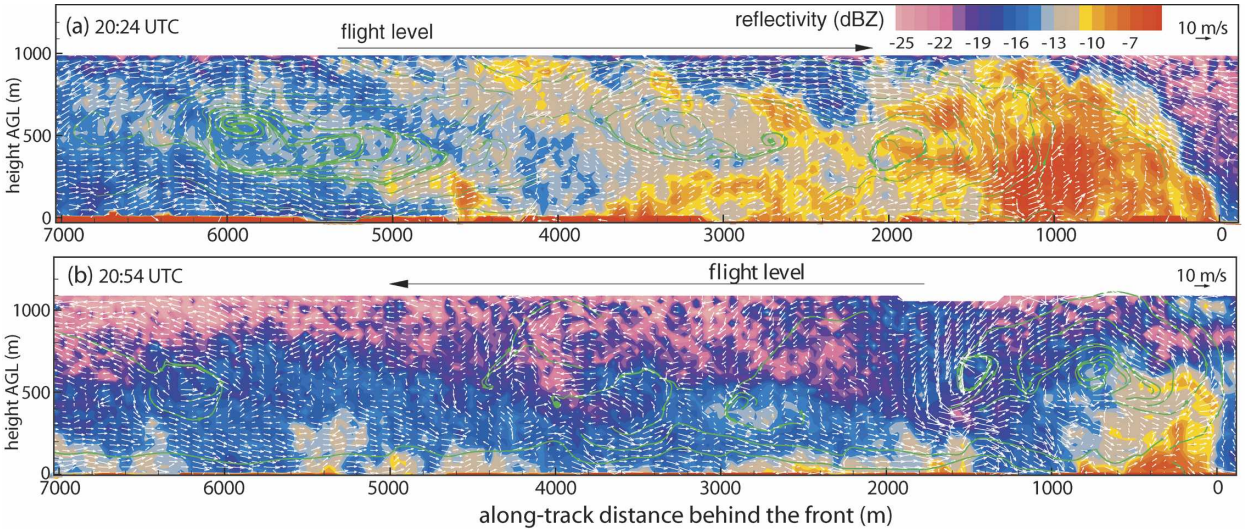

FIG. 13. As in Fig. 10, but the flight level is ~1.1 km and at (a) 2000:24 UTC (the flight leg orientation is 344°–164°) and (b) 2000:54 UTC (the flight leg orientation is 300°–120°).

this streamline encounters V values up to 18 m s^{-1}; thus the pressure deficit there is 2 mb according to (6). Dynamically induced pressure deficits of this magnitude have been numerically simulated, both in strong KH vortices and in the density current head (Xue et al. 1997). In IHOP flight-level pressure perturbations could not be measured accurately because the exact altitude of the aircraft was unknown, but at $x = 1200$ m the difference between pressure altitude (MSL) and attitude-corrected radar altitude (AGL) suddenly increased by ~15 m. This can be attributed to the nonhydrostatic pressure deficit, if the local terrain is level.

A continuous, broad (~500–800 m wide) updraft slopes over the incoming density current (Fig. 12c), as in Fig. 11. The updraft speed averages 4 m s^{-1} and increases upward, which implies convergent flow according to airmass continuity. To the rear of the updraft belt is an equally continuous, sloping downdraft averaging -1 m s^{-1}. This vertical velocity couplet is consistent with a narrow belt of positive vorticity with mean (peak) values similar to those obtained for Fig. 11, namely 0.05 s^{-1} (0.17 s^{-1}). The vorticity data in Figs. 11c and 12d yield an average shear $|\nabla \mathbf{v}|$ of 0.1 s^{-1} along the sloping frontal boundary, over a distance Δx of 100 m. Thus Ri $\cong$ 0.1. This compares well with the sounding-estimated value (section 4), confirming that KH instability is expected.

The three transects shown so far have focused on the density current head and the major vortex behind it. We now look farther behind the leading edge to examine how the KH billows evolve. These billows clearly play a major role in the mixing and entrainment of the gravity current with the lifted prefrontal CBL. The flow field transects of Fig. 13, as well as the echo structure shown in Fig. 8, indicate that rearward of the head the amplitude of the KH billows decreases, and thus the entrainment/detrainment along the density interface decreases. Figure 13a is the same transect as Fig. 12. The transect in Fig. 13b was flown about 30 min later.

Several breaking KH waves are evident in the reflectivity pattern in Fig. 8. Such waves are associated with rotating flow, as can be seen for instance at $x = 3600$ m and $x = 6200$ m in Fig. 13b. The wave-breaking process appears complex, with small vortices superimposed on large ones, many of them sheared out by the wind shear at the density interface. The circulations in the 2024 UTC transect (Fig. 13a) are 300–600 m deeper than the 2054 UTC transect, suggesting that the density current depth decreases during this interval. In fact downdrafts dominate in the later transect, at least to the rear of the head (not shown), indicating a subsidence of the gravity current top at this stage. The echo strength also decreases substantially (Fig. 13).

At the largest scale, both transects in Fig. 13 can be viewed as an amplitude-ordered series of three large echo protrusions sloping upward in the direction of the shear vector (toward the northwest, i.e., from right to left), each associated with a closed circulation in a front-relative frame of reference. A similar image emerges in the field horizontal vorticity field (not shown), when one ignores the small-scale features: three sloping swaths of positive vorticity are present, some 1500–2000 m apart along the flight track. A similar wavelength can be seen in Fig. 8: the dominant vortices near the head may be shorter (~1000 m), but the

wavelength increases to the rear, as mentioned in section 4.

Finally, we note an unusual, almost upright leading edge at 2054 UTC, both in the velocity and the reflectivity fields. This may be a transient configuration; however the reflectivity field seems to have adjusted to the flow field, which takes some time. The density current head is actually part of a large, strong circulation, with a broad, deep downdraft located 800–1900 m behind the nose. This circulation is reminiscent of a cutoff vortex sometimes observed in density currents (e.g., Simpson et al. 1977). It is not clear whether the cold air in this large vortex is actually separated from the rear-inflow current; however in situ observations elsewhere (e.g., Figs. 7 and 8) indicate that the prefrontal air may be drawn close to the ground in the downdraft behind the head. The amount of flow restriction or even separation of the head may vary continuously, with the cutoff in Fig. 13b more complete than the one shown in Fig. 7. Onboard forward-looking video imagery confirms that the weak echo near flight level, above the head in Fig. 13b, is a cloud that developed about 50 s before the overflight. This cloud was not an arc (shelf) cloud above the density current. Rather, it appeared as a rapidly evolving, highly sheared roll cloud within the cold air. At flight level the cloud encounter was marked by a 500-m-wide, 3–4 m s^{-1} strong updraft. This cloud development suggests that the erect updraft at the leading edge of the large cutoff vortex in Fig. 13b was growing, and this may be consistent with the observed thinning of the trailing density current body. It is not known whether this evolution is sustained or transient, nor whether it is local or widespread.

6. Discussion

The WCR data have been used to describe the kinematics of a density current at unprecedented detail. All four VPDD transects shown in Figs. 10–13, and the longer transect of Fig. 8, epitomize the cold front as an atmospheric density current at the scales shown here. This includes a "nose" and a well-defined "head," front-relative rear-to-front inflow in the cold air, an "undercurrent," rearward acceleration of the ambient warm air over the current, and strong shear across the interface leading to the formation of a series of KH vortices, which are responsible for the intense turbulence observed in the wake (Fig. 1). These observations are consistent with laboratory experiments (e.g., Simpson 1969), numerical simulations (e.g., Droegemeier and Wilhelmson 1987; Xue 2002), and observations in the atmosphere (e.g., Wakimoto 1982; Mueller and Carbone 1987). The amplitude of the leading billows is remarkably large, sometimes penetrating to near the ground. Numerical simulations (Xue et al. 1997) show that large billows just to the rear of the head occur especially when the wind shear is weak, or "reversed" (i.e., the vorticity of the ambient shear is in the same direction as the baroclinically generated vorticity). It is clear from the three soundings taken just in front of the cold front that little wind shear exists in the CBL up to the stable layer (~2.2 km AGL) and even higher (Fig. 9). The mean shear in the lowest 2.2 km is reversed in two of the three soundings in Fig. 9.

According to KH instability theory, waves form on the density current head, they grow into billows, and dissipate into turbulence farther to the rear (Thorpe 1973). Observations in a thunderstorm outflow (Mueller and Carbone 1987) and numerical simulations (Droegemeier and Wilhelmson 1987; Xue et al. 1997; Xue 2000) have confirmed the rearward advection of KH billows. Our airborne observations are too discontinuous ($\Delta t \sim 10$ min), and the movement and evolution of billows too rapid, to identify billows in successive transects and to determine their front-relative speed.

The height and forward slope of the head also vary considerably, suggesting rapid temporal changes and/or large alongfront differences. The head is usually rearward-sloping, yet in Fig. 13b it is remarkably upright. Laboratory studies indicate that the density current nose (i.e., the forward-most protrusion) is sometimes elevated, due to surface friction (Simpson 1987). This may be the case for the transects shown in Figs. 8 and 12; it certainly is the case in Fig. 13b. The leading head is not necessarily the deepest pocket of cold air (e.g., Fig. 7), and may evolve into a cutoff vortex (Fig. 13b).

Clearly the strong wind shear results in the breakdown of the horizontal interface between the warm and cold air through a series of large-amplitude KH vortices (Fig. 8). Our observations show that the solenoidally induced vortices form quite early: horizontal vorticity, generated along the sloping front of the density current head, can break up into eddies along this sloping front (e.g., Fig. 10). These vortices can be rather large in size, occupying much of the density current depth, and possibly temporarily cutting off the leading vortex from the trailing cold-air mass. WCR data (e.g., Fig. 8) and visual observations of stratus cloud bands aligned with the cold front indicate that the KH billows decay to low-amplitude gravity waves on the body of the density current farther to the rear. These waves are lee-type waves forced by the gravity current that acts as an obstacle to the opposing prefrontal flow (e.g., Ralph et al. 1993).

7. Conclusions

Airborne Doppler radar data, as well as coincident aircraft data, have been used to describe the vertical structure of a cold front intersecting with a dryline and penetrating into a relatively deep, weakly capped, and weakly sheared convective boundary layer. Frontogenesis due to differential surface heating over the central Great Plains resulted in a well-defined cold front, which was shallow compared to the prefrontal CBL. Because the dryline was not associated with a buoyancy gradient, its collision with the cold front had no significant dynamic impact on the cold front. Deep convection did break out, but clearly ahead of the cold front, at least in the region of detailed observations.

The radar data depict the cold front as an atmospheric density current at unprecedented detail (~40 m). The echo structure and dual-Doppler-inferred airflow in the vertical plane reveal typical features such as a nose, a head, a rear-inflow current, an undercurrent, and a current of rising prefrontal air that accelerates into a rearward flow over the head. The width of this updraft is nearly the same as the depth of the density current body, ~800 m, and over this width it is ~4 m s^{-1} strong. The two-dimensional cross-frontal structure, including the frontal slope and the elevation of the nose, is highly variable in time and/or alongfront distance. Along a sloping zone marking the leading edge of the head, horizontal vorticity is baroclinically generated, averaging ~0.05 s^{-1}. The associated wind shear triggers Kelvin–Helmholtz waves that rapidly amplify and break. The KH billows behind the head have a large diameter, sometimes occupying much of the depth of the density current, leading to strong entrainment of prefrontal air deep down into the density current. On one occasion the head even seems to become cut off from the density current body. Lee-type gravity waves occur on the cold-frontal surface to the rear of the KH billows. The density current also triggers undulations in the cap near 2.0–2.4 km AGL, a layer stable enough to prevent deep convection, notwithstanding the strong updraft over the cold front.

This study describes the kinematic structure of the cold-frontal density current and its mesoscale environment. It does not quantitatively assess dynamical processes, especially those of vorticity generation and breakup. This requires knowledge of the pressure and buoyancy distribution. Further plans include a retrieval of these fields assuming dynamical consistency with the observed flow field, subject to lateral boundary conditions provided by soundings. This technique has been used before (e.g., Roux et al. 1984; Lin et al. 1986; Geerts and Hobbs 1991), but not at this resolution.

Acknowledgments. This work is support by the National Science Foundation, Grant ATMS0129374. David Leon provided the initial WCR dual-Doppler syntheses of the cold front. Larry Oolman processed the King Air and sounding data. Roger Wakimoto provided us with an early version of the Wakimoto et al. (2006) paper. While this study focuses on WCR and King Air data, it relies on data collected by all IHOP_2002 participants, especially the Learjet, SMART-R, ELDORA, and mobile mesonet crews.

APPENDIX A

Dual-Doppler Analysis Technique

A total of four antennas are mounted on the UWKA: two point down along the vertical plane normal to that of the wings (Fig. 1); the other two point sideways to the starboard side of the aircraft. The first pair allows for the retrieval of velocities on a vertical plane aligned with the aircraft track (VPDD); the second scans a horizontal plane (side and forward-side antennas, yielding horizontal-beam dual-Doppler, which was not used in IHOP_2002). One of the horizontal beams can be redirected upward, thus allowing for the up/down profiling mode (Fig. 1). Obviously, the effective plane of scan will also depend on the aircraft attitude.

The conceptual basis of the airborne dual-Doppler synthesis is well established (Jorgensen et al. 1983; Ray et al. 1985; Heymsfield et al. 1996). The radar radial velocities from one pair of beams (antennas) are corrected for aircraft motion and synthesized to provide orthogonal components of the scatterers' mean velocity in a given illuminated volume (Fig. A1). The synthesis requires a merging of the radial velocities onto a common grid. This can be carried out in two different ways according to the type of flight pattern adopted. In case of large attitude Kelvin–Helmholtz variations producing a curved aircraft track, three-dimensional (3D) radar-scanned surfaces are computed. The grid layout, in this case, consists of a complex undulating surface generated by following the aircraft trajectory and attitude in a 3D space. For sufficiently straight and level flight legs, the dual-Doppler analysis can be simplified by projecting the 3D data from the two beams onto a mean geometrical plane, which approximates a vertical (or horizontal) plane. The latter method can be used for 24 May, because all cold-front transects were straight and level by design. A full description of the gridding methodology is beyond the scope of this paper; here it will suffice to state that the grid is constructed based on the aircraft track relative to a reference frame advecting with the mean wind (Gal-Chen 1982) and on the desired grid-cell dimensions. Data points coming from the

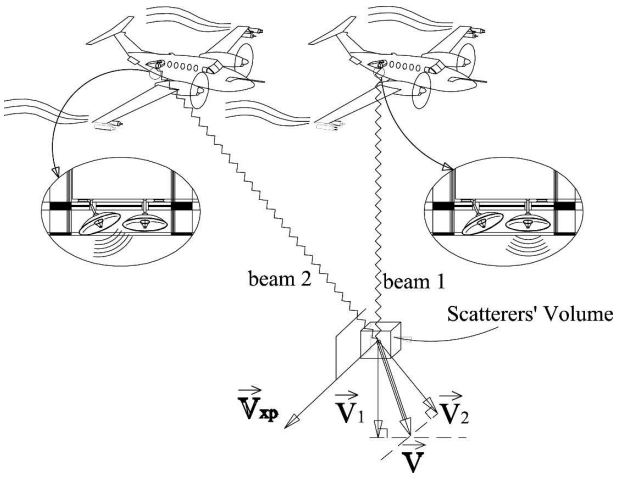

FIG. A1. Dual-Doppler concept: a given scatterer's volume is illuminated nearly simultaneously by two beams of different incidence. Here V_1 and V_2 are the Doppler mean radial velocities deprived of aircraft motion; V_{xp} denotes the unmeasured "cross plane" component normal to the plane of the beams.

two beams are then assigned to the grid cells based on their spatial position and weighted according to selected criteria. Doppler velocity data are unfolded to resolve frequency aliasing, if any, before proceeding with the dual-Doppler calculations.

These calculations are based on a *velocity inverse decomposition* problem, consisting of the retrieval of the velocity vector that decomposes in the radar-measured components for every grid cell. Since the true scatterer velocity is a 3D vector, but there are only two independently measured components (one per beam direction), one may hope to resolve with sufficient accuracy just the velocity on the plane determined by the beam directions. However, in order to achieve a good determination of this 2D vector, an estimate of the *cross-plane* component, the vector normal to the solution plane (see below), is necessary (Fig. A1). For instance, when the aircraft rolls 3° under a 10 m s^{-1} cross-track wind, then this wind causes a 0.5 m s^{-1} error in the vertical velocity that is obtained by projecting the slant-vertical vector onto the vertical plane. For this purpose an *external* guess of the 3D (or at least horizontal) wind vector is also employed. This can be inferred from in situ gust probe measurements, or a proximity sounding. The sought velocity **v** associated with any given grid cell is calculated by solving a linear system of equations:

$$\begin{cases} \mathbf{v} \cdot \mathbf{b}_1 = c_1 \\ \mathbf{v} \cdot \mathbf{b}_2 = c_2 \\ \quad \vdots \\ \mathbf{v} \cdot \mathbf{b}_n = c_n \end{cases}, \tag{A1}$$

where $\mathbf{b}_k$ represent the beam unit vectors associated with n data points belonging to a grid cell, c_k are the corresponding measured Doppler radial velocities (positive away from the radar), and · stands for a dot product. The unknown vector **v** is the mean absolute (ground relative) velocity of the scatterers in the volume. A prescribed mean wind velocity can be subtracted at a later stage, for example, to investigate the front-relative kinematic field (appendix B). Weighting can be applied to each equation in (A1) based on different criteria, for example, known measured Doppler velocity error. All the vector fields presented in this paper are calculated using a uniform weighting.

Given that the data points are from two independent measurements (two beams) and that the radar resolution volume is normally only a fraction of the selected grid resolution, the set of Eqs. (A1) can be described as overdetermined but rank deficient. This type of problem can be solved with a generalized weighted least squares method, such as the singular value matrix decomposition (SVD) (Golub and Van Loan 1989, 241–248; Nash 1990, 19–42). The SVD solution of system (A1) can be expressed as follows:

$$\mathbf{v} = [\mathbf{V}][\mathbf{W}]^{-1}[\mathbf{U}]^{\mathrm{T}}\{\mathbf{c}\}, \tag{A2}$$

where {**c**} is the vector of the measured radial velocities and the product $[\mathbf{V}][\mathbf{W}]^{-1}[\mathbf{U}]^{\mathrm{T}}$ is the *pseudoinverse* matrix of [**B**] (the system matrix of the beam unit vector coefficients): [**U**] is a ($n \times 3$) matrix whose columns are orthogonal, [**W**] is a (3×3) diagonal matrix of singular values w_{jj}, and [**V**] is a (3×3) orthonormal matrix. An important property of the SVD is that the columns of [**U**], whose same numbered elements w_{ii} are nonzero, represent an orthonormal set of basis vectors that span the solution space, that is, the range of [**B**]. Furthermore, the columns of [**V**], whose same numbered elements w_{ii} are zero, represent an orthonormal set of basis vectors that span the null space. This property may be used to add the external wind information to the solution and thus improve its accuracy. The null space, in the dual-Doppler analysis, can be represented by the unit vector normal to the *solution plane*. The solution plane, from a geometrical point of view, is the best fit, in the least squares sense, of all the planes determined by the beam unit vector pairs.

APPENDIX B

Display of Velocity Fields

The flow fields shown in the VPDD transects (Figs. 10–13) are relative to the cold front. We assume a frontal motion of 6.9 m s^{-1} toward 148°, based on a time

series of SMART-R reflectivity images, ELDORA data shown in Wakimoto et al. (2006), and UWKA/WCR transects. This corresponds well with the theoretical speed of a density current (Simpson and Britter 1980),

$$u_{\mathrm{DC}} = \mathrm{Fr}\sqrt{gh\frac{\Delta\rho}{\rho}} + U_a, \tag{B1}$$

where U_a is the ambient mean flow (positive when directed away from cold air), h is defined in Fig. 1, $\Delta\rho$ is the air density difference, and Fr is the Froude number $\mathrm{Fr} = U_a/Nh$, and N the Brunt–Väisälä frequency. Using $U_a = -3.5\ \mathrm{m\ s^{-1}}$ (the average prefrontal flow normal to the front, in the lowest 2 km, according to three soundings shown in Fig. 9), $N = 0.005\ \mathrm{s^{-1}}$ (from the same three prefrontal soundings, in the lowest 2 km), $h = 800$ m (section 4), and $\Delta\rho = -\Delta T_v = 4$ K (Fig. 8 and other transects, estimated over a distance of ~10 km behind the cold front), we obtain $U_{\mathrm{DC}} = 6.7\ \mathrm{m\ s^{-1}}$.

The streamlines shown in the VPDD transects (Figs. 10–13) are, by definition, locally tangent to the instantaneous vectors in the frame of reference moving with the cold front. These streamlines are initiated at arbitrary points, and then integrated through the field.

The vectors shown are undersampled, to enhance legibility of the wind field. They are not filtered nor smoothed; however the streamlines are obtained based on a smoothed velocity field. Smoothing is used also in the calculation of the horizontal vorticity. A Laplace smoothing technique is used, with a dampening factor of 0.3. This technique minimizes the sum of the squares of the velocity component partial derivatives. This results in a 2D weighted moving average that dampens without completely removing the peaks in the original field. Four smoothing passes are applied in the two deep transects (Figs. 10 and 11), and two passes in the two shallow transects (Figs. 12 and 13).

REFERENCES

Abbs, D. J., and W. L. Physick, 1992: Sea-breeze observations and modelling: A review. *Aust. Meteor. Mag.,* **41,** 7–19.

Benjamin, T. B., 1968: Gravity currents and related phenomena. *J. Fluid Mech.,* **31,** 209–248.

Bond, N. A., and R. G. Fleagle, 1985: Structure of a cold front over the ocean. *Quart. J. Roy. Meteor. Soc.,* **111,** 739–759.

——, and M. A. Shapiro, 1991: Research aircraft observations of the mesoscale and microscale structure of a cold front over the eastern Pacific Ocean. *Mon. Wea. Rev.,* **119,** 3080–3094.

Britter, R. E., and J. E. Simpson, 1978: Experiments on the dynamics of a gravity current head. *J. Fluid Mech.,* **88,** 223–240.

Bromwich, D. H., J. F. Carrasco, and C. R. Stearns, 1992: Satellite observations of katabatic-wind propagation for great distances across the Ross Ice Shelf. *Mon. Wea. Rev.,* **120,** 1940–1949.

Carbone, R. E., 1982: A severe frontal rainband. Part I. Stormwide hydrodynamic structure. *J. Atmos. Sci.,* **39,** 258–279.

Charba, J., 1974: Application of gravity current model to analysis of squall-line gust front. *Mon. Wea. Rev.,* **102,** 140–156.

Clarke, R. H., 1961: Mesostructure of dry cold fronts over featureless terrain. *J. Atmos. Sci.,* **18,** 715–735.

Drake, V. A., and R. A. Farrow, 1988: The influence of atmospheric structure and motions on insect migration. *Annu. Rev. Entomol.,* **33,** 183–210.

Droegemeier, K. K., and R. B. Wilhelmson, 1987: Numerical simulation of thunderstorm outflow dynamics. Part I: Outflow sensitivity experiments and turbulence dynamics. *J. Atmos. Sci.,* **44,** 1180–1210.

Gal-Chen, T., 1982: Errors in fixed and moving frame of references: Applications for conventional and Doppler radar analysis. *J. Atmos. Sci.,* **39,** 2279–2300.

Garratt, J. R., 1988: Summertime cold fronts in Southeast Australia—Behavior and low-level structure of main frontal types. *Mon. Wea. Rev.,* **116,** 636–649.

Geerts, B., and P. V. Hobbs, 1991: The organization and structure of clouds and precipitation on the mid-Atlantic coast of the United States. Part IV: Retrieval of thermodynamic and cloud microphysical structures of a frontal rainband from Doppler radar data. *J. Atmos. Sci.,* **48,** 1287–1305.

—— and Q. Miao, 2005: The use of millimeter Doppler radar echoes to estimate vertical air velocities in the fair-weather convective boundary layer. *J. Atmos. Oceanic Technol.,* **22,** 225–246.

Goff, C. R., 1976: Vertical structure of thunderstorm outflows. *Mon. Wea. Rev.,* **104,** 1429–1440.

Golub, G. H., and C. F. Van Loan, 1989. *Matrix Computations*. 2d ed. The John Hopkins University Press, 623 pp.

Hakim, G. J., 1992: The eastern United States side-door cold front of 22 April 1987: A case study of an intense atmospheric density current. *Mon. Wea. Rev.,* **120,** 2738–2762.

Heymsfield, G. M., and Coauthors, 1996: The EDOP radar system on the high-altitude NASA ER-2 aircraft. *J. Atmos. Oceanic Technol.,* **13,** 795–809.

Hobbs, P. V., and P. O. G. Persson, 1982: The mesoscale and microscale structure and organization of clouds and precipitation in midlatitude cyclones. Part V: The substructure of narrow cold-frontal rainbands. *J. Atmos. Sci.,* **39,** 280–295.

Holton, J. R., 2004: *An Introduction to Dynamic Meteorology*. 4th ed. Academic Press, 535 pp.

Houze, R. A., 1993: *Cloud Dynamics*. Academic Press, 573 pp.

Intrieri, J. M., A. J. Bedard, and R. M. Hardesty, 1990: Details of colliding thunderstorm outflows as observed by Doppler lidar. *J. Atmos. Sci.,* **47,** 1081–1099.

Kingsmill, D. E., and A. Crook, 2003: An observational study of atmospheric bore formation from colliding density currents. *Mon. Wea. Rev.,* **131,** 2985–3002.

Koch, S. E., and W. L. Clark, 1999: A non-classical cold front observed during COPS-91: Frontal structure and the process of severe storm initiation. *J. Atmos. Sci.,* **56,** 2862–2890.

Jorgensen, D. P., P. H. Hildebrand, and C. L. Frush, 1983: Feasibility test of an airborne pulse-Doppler meteorological radar. *J. Appl. Meteor.,* **22,** 744–757.

Lemaitre, Y., G. Scialom, and P. Amayenc, 1989: A cold frontal rainband observed during the LANDES-FRONTS 84 experiment: Mesoscale and small-scale structure inferred from dual-Doppler radar analysis. *J. Atmos. Sci.,* **46,** 2215–2235.

Lin, Y. J., T. C. Wang, and J. H. Lin, 1986: Pressure and temperature perturbations within a squall-line thunderstorm derived

from SESAME dual-Doppler data. *J. Atmos. Sci.,* **43,** 2302–2327.

Liu, C. H., and M. W. Moncrieff, 2000: Simulated density currents in idealized stratified environments. *Mon. Wea. Rev.,* **128,** 1420–1437.

Mahoney, W. P., 1988: Gust front characteristics and the kinematics associated with interacting thunderstorm outflows. *Mon. Wea. Rev.,* **116,** 1474–1492.

Miller, L. J., M. A. LeMone, W. Blumen, R. L. Grossman, N. Gamage, and R. J. Zamora, 1996: The low-level structure and evolution of a dry arctic front over the central United States. Part I: Mesoscale observations. *Mon. Wea. Rev.,* **124,** 1648–1675.

Mueller, C. K., and R. E. Carbone, 1987: Dynamics of a thunderstorm outflow. *J. Atmos. Sci.,* **44,** 1879–1898.

Nash, J. C., 1990: *Compact Numerical Methods for Computers: Linear Algebra and Function Minimisation.* 2d ed. Adam Hilger, 498 pp.

Nielsen, J. W., and P. P. Neilley, 1990: The vertical structure of New England coastal fronts. *Mon. Wea. Rev.,* **118,** 1793–1807.

Pazmany, A., R. McIntosh, R. Kelly, and G. Vali, 1994: An airborne 95 GHz dual-polarized radar for cloud studies. *IEEE Trans. Geosci. Remote Sens.,* **32,** 731–739.

Pedgley, D. E., 1982: *Windborne Pest and Diseases: Meteorology of Airborne Organisms*. Wiley, 284 pp.

Ralph, F. M., C. Mazaudier, M. Crochet, and S. V. Venkateswaran, 1993: Doppler sodar and radar wind-profiler observations of gravity-wave activity associated with a gravity current. *Mon. Wea. Rev.,* **121,** 444–463.

Ray, P. S., D. P. Jorgensen, and S.-L. Wang, 1985: Airborne Doppler radar observations of a convective storm. *J. Climate Appl. Meteor.,* **24,** 688–698.

Rotunno, R., J. B. Klemp, and M. L. Weisman, 1988: A theory for strong, long-lived squall lines. *J. Atmos. Sci.,* **45,** 463–485.

Roux, F., J. Testud, M. Payen, and B. Pinty, 1984: West African squall-line thermodynamic structure retrieved from dual-Doppler radar observations. *J. Atmos. Sci.,* **41,** 3104–3121.

——, V. Marécal, and D. Hauser, 1993: The 12/13 January 1988 narrow cold-frontal rainband observed during MFDP/FRONTS 87. Part I: Kinematics and thermodynamics. *J. Atmos. Sci.,* **50,** 951–974.

Russell, R. W., and J. W. Wilson, 1997: Radar-observed "fine lines" in the optically clear boundary layer. Reflectivity contributions from aerial plankton and its predators. *Bound.-Layer Meteor.,* **82,** 235–262.

Schoenberger, L. M., 1984: Doppler radar observation of a land-breeze cold front. *Mon. Wea. Rev.,* **112,** 2455–2464.

Scorer, R. S., 1997. *Dynamics of Meteorology and Climate*. Wiley, 686 pp.

Shapiro, M. A., 1984: Meteorological tower measurements of a surface cold front. *Mon. Wea. Rev.,* **112,** 1634–1639.

——, T. Hampel, D. Rotzoll, and F. Mosher, 1985: The frontal hydraulic head: A micro-α scale ($\sim$1 km) triggering mechanism for mesoconvective weather systems. *Mon. Wea. Rev.,* **113,** 1166–1183.

Simpson, J. E., 1969: A comparison between laboratory and atmospheric density currents. *Quart. J. Roy. Meteor. Soc.,* **95,** 758–765.

——, 1987: *Gravity Currents: In the Environment and the Laboratory*. Ellis Horwood, 244 pp.

——, and R. E. Britter, 1980: A laboratory model of an atmospheric mesofront. *Quart. J. Roy. Meteor. Soc.,* **106,** 485–500.

——, D. A. Mansfield, and J. R. Milford, 1977: Inland penetration of sea-breeze fronts. *Quart. J. Roy. Meteor. Soc.,* **103,** 47–76.

Smith, R. K., and M. J. Reeder, 1988: On the movement and low-level structure of cold fronts. *Mon. Wea. Rev.,* **116,** 1927–1944.

Thorpe, S. A., 1973: Experiments on instability and turbulence in a stratified shear flow. *J. Fluid Mech.,* **61,** 731–751.

Trier, S. B., D. B. Parsons, and T. J. Matejka, 1990: Observations of a subtropical cold front in a region of complex terrain. *Mon. Wea. Rev.,* **118,** 2449–2470.

Vaughn, C. R., 1985: Birds and insects as radar targets: A review. *Proc. IEEE,* **73,** 205–227.

Wakimoto, R. M., 1982: The life cycle of thunderstorm gust fronts as viewed with Doppler radar and rawinsonde data. *Mon. Wea. Rev.,* **110,** 1060–1082.

——, and B. L. Bosart, 2000: Airborne radar observations of a cold front during FASTEX. *Mon. Wea. Rev.,* **128,** 2447–2470.

——, H. V. Murphey, E. V. Browell, and S. Ismail, 2006: The "triple point" on 24 May 2002 during IHOP. Part I: Airborne Doppler and LASE analyses of the frontal boundaries and convection initiation. *Mon. Wea. Rev.,* **134,** 231–250.

Weckwerth, T. M., and Coauthors, 2004: An overview of the International H_2O Project (IHOP_2002) and some preliminary highlights. *Bull. Amer. Meteor. Soc.,* **85,** 253–277.

Wilson, J. W., T. M. Weckwerth, J. Vivekanandan, R. M. Wakimoto, and R. W. Russell, 1994: Boundary-layer clear-air radar echoes: Origin of echoes and accuracy of derived winds. *J. Atmos. Oceanic Technol.,* **11,** 1184–1206.

Wurman, J., and S. Gill, 2000: Finescale radar observations of the Dimmitt, Texas (2 June 1995), tornado. *Mon. Wea. Rev.,* **128,** 2135–2164.

Xue, M., 2000: Density current in two-layer shear flows. *Quart. J. Roy. Meteor. Soc.,* **126,** 1301–1320.

——, 2002: Density currents in shear flows: Effects of rigid lid and cold-pool internal circulation, and application to squall line dynamics. *Quart. J. Roy. Meteor. Soc.,* **128,** 47–74.

——, and W. J. Martin, 2006: A high-resolution modeling study of the 24 May 2002 dryline case during IHOP. Part I: Numerical simulation and general evolution of the dryline and convection. *Mon. Wea. Rev.,* **134,** 149–171.

——, Q. Xu, and K. K. Droegemeier, 1997: A theoretical and numerical study of density currents in nonconstant shear flows. *J. Atmos. Sci.,* **54,** 1998–2019.